AAS 21-254

SPACECRAFT TERRAIN RELATIVE NAVIGATION WITH SYNTHETIC APERTURE RADAR

Bryan S. Pogorelsky[*], Renato Zanetti[†], Jingyi Chen[‡], and Scott Jenkins[§]

Situations can arise when a spacecraft cannot rely on external signals for navigation and must use onboard instruments to determine its position, velocity, and attitude in orbit. A spacecraft terrain relative navigation system is presented relying on measurements obtained from a synthetic aperture radar that are fused with inertial measurements and attitude determination system data in a multiplicative extended Kalman filter. The method of processing the SAR images to retrieve measurements for the navigation filter is shown, including autofocusing and image geolocation steps. Monte Carlo simulation results are presented in which actual filter performance is compared to predicted filter performance. Specifically, two test cases, with varied initial SAR antenna misalignment uncertainty, demonstrate that the SAR based terrain relative navigation system produces consistent state estimates and successfully bounds, or in some instances, significantly reduces the navigation uncertainty of the spacecraft throughout its trajectory by up to 98%.

INTRODUCTION

When a spacecraft cannot rely on ground stations or global navigation satellite systems, such as GPS, terrain relative navigation (TRN) is a method that can be employed to obtain accurate onboard navigation solutions. The basic functionality of TRN is to aid inertial navigation systems (INS) by providing relative position or bearing information to known surface features.

Data acquired from various sensor types have been used for TRN, including radar altimeters as in the case of the Terrain Contour Matching System (TERCOM),[1] passive optical cameras employed in the Autonomous Precision Landing Navigation system (APLNav),[2] and LIDAR in NASA's Autonomous Landing Hazard Avoidance Technology (ALHAT) project for lunar landing.[3] *A priori* reference maps, such as digital elevation maps (DEMs) or optical images with scaling information, are required to perform TRN. These reference maps can be created pre-flight or during the mission as was done with the Dawn spacecraft.[4]

All sensors have their respective advantages and disadvantages. For example, optical imagery provides large amounts of spatial coverage but can be negatively impacted by adverse light, cloud, or weather conditions. Radar altimeters, while being able to function in most weather and lighting conditions, require long contours to be collected for geolocation.[5] Technologies such as flash LIDAR can collect a grid of range measurements to be used for correlation with DEMs, but are generally limited in their effective range when used for TRN. The ALHAT flash LIDAR for example has an operational range of 1800 m to 20 km when the number of illuminated pixels is reduced from 128×128 to 11×11.[6] This range is not sufficient for performing terrain relative navigation at altitudes experienced in low Earth orbit. Synthetic Aperture Radar (SAR) is an imaging radar that is widely used for remote sensing science applications as well as military surveillance and reconnaissance activities. Using SAR for navigation purposes presents some compelling advantages over the sensors outlined above. SAR receives radar echoes independent of lighting or weather conditions from large distances and with high spatial resolution. This has been successfully demonstrated in a variety of orbital

[*]Graduate Research Assistant, Aerospace Engineering and Engineering Mechanics, The University of Texas at Austin
[†]Assistant Professor, Aerospace Engineering and Engineering Mechanics, The University of Texas at Austin
[‡]Assistant Professor, Aerospace Engineering and Engineering Mechanics, The University of Texas at Austin
[§]Engineer, Dept. 5322 (NPC and Systems Integration), Sandia National Laboratories.

applications such as Seasat,[7] the Shuttle Radar Topography Mission (SRTM),[8] and Sentinel-1.[9] SAR based navigation blends many of the advantages of flash LIDAR, radar altimetry, and optical sensors in that it can collect image-like data with range information from large distances and in many environmental conditions.

Previous studies have been conducted in the use of SAR for terrain relative navigation. Bevington and Marttila[10] proposed obtaining aircraft position updates for an inertial navigation system with imagery gathered from a synthetic aperture radar. A dynamic programming approach was implemented to match linear features (such as roads) from optical images to corresponding linear features in the SAR images. To test the performance of this system, open-loop navigation and feature prediction/extraction performance were evaluated separately. Open-loop navigation refers to the fact that SAR sensor-based measurement updates were modeled as point fixes with errors and were not obtained from SAR images derived from an INS solution. This resulted in position accuracies on the order of tens of meters. An important caveat in SAR image processing is that precise knowledge of platform velocity and pointing are needed to produce high-quality images, making closed-loop (where SAR based measurements are dependent on INS solutions) image formation a challenge. Paschall and Layne[11] investigated an INS, GPS, and SAR targeting system where SAR derived measurements were fed into a Kalman filter. Monopulse measurements were also integrated into this system to provide complete angle information to targets. Additionally, no image correlation was performed, thus accurate knowledge of landmark locations was needed for SAR aided navigation to be effective. More recently, work by Doerry[12] and Doerry et al.[13] describe methods of using SAR images to estimate IMU heading errors and radar velocity respectively, where the information could ultimately be fed into a navigation filter.

This works seeks to develop an approach to SAR based terrain relative navigation for space based platforms. Additionally, this is done without the use of external aiding, namely GPS, while removing some limitations of the studies mentioned above such as feature matching only being applied to linear features. Most importantly, closed-loop navigation simulations are performed where SAR derived measurements are reliant on the navigation solution, and conversely, the navigation solution is reliant on the SAR derived measurements.

SYSTEM OVERVIEW

The proposed system consists of four major steps: SAR image formation, SAR image geolocation, INS state propagation, and finally an EKF measurement update. Figure 1 below shows the system architecture and flow of the navigation process.

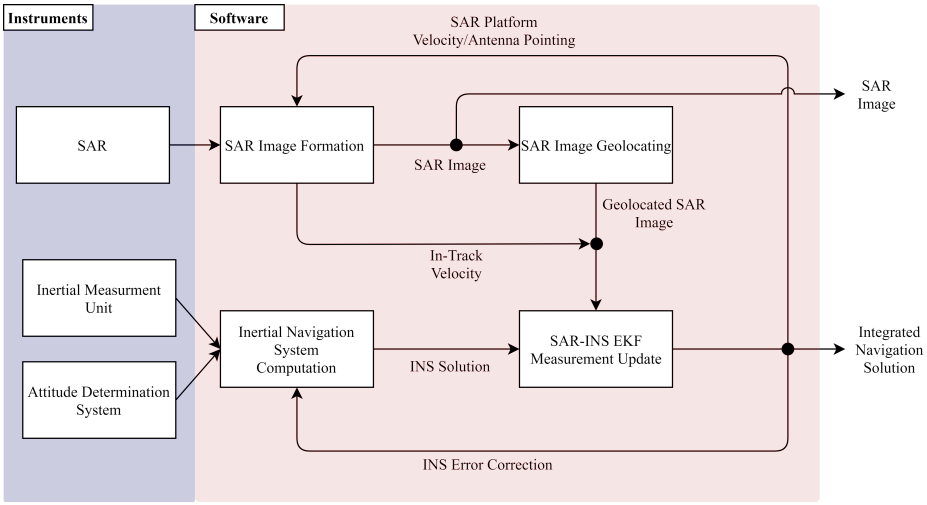

Figure 1: Integrated SAR-INS architecture

A multiplicative extended Kalman filter (MEKF) is used with states for spacecraft position, velocity, and SAR antenna misalignment. To estimate in-track velocity errors, an autofocusing algorithm (with in-track velocity as the tuning parameter) is implemented to form a well-focused SAR image. Geolocation is done by co-registering the center pixel of the SAR image with a geocoded reference SAR image using a feature matching algorithm. The Earth-centered, Earth-fixed (ECEF) coordinate of the center pixel of the image is then extracted along with the slant range to that pixel. From the autofocusing step, an estimate of the spacecraft's in-track velocity is used as an additional measurement. These are then utilized in the MEKF to produce the final navigation solution.

SAR IMAGE FORMATION

SAR Overview

SAR systems send out pulses of sequential electromagnetic waves and collect backscattered echoes. Every transmission/reception corresponds to different positions due to the movement of the platform; an appropriate coherent combination of the received signals creates the "synthetic aperture". This synthetic aperture is much larger than the physical antenna length, allowing it to achieve high spatial resolution.[14] For the purposes of this paper, all SAR data is being collected in a stripmap mode. This means that the antenna stays fixed relative to the moving platform and is not being actively gimbaled during flight to "spotlight" a specific area on the ground. A graphic of the SAR imaging geometry can be seen below in Figure 2. The two properties of

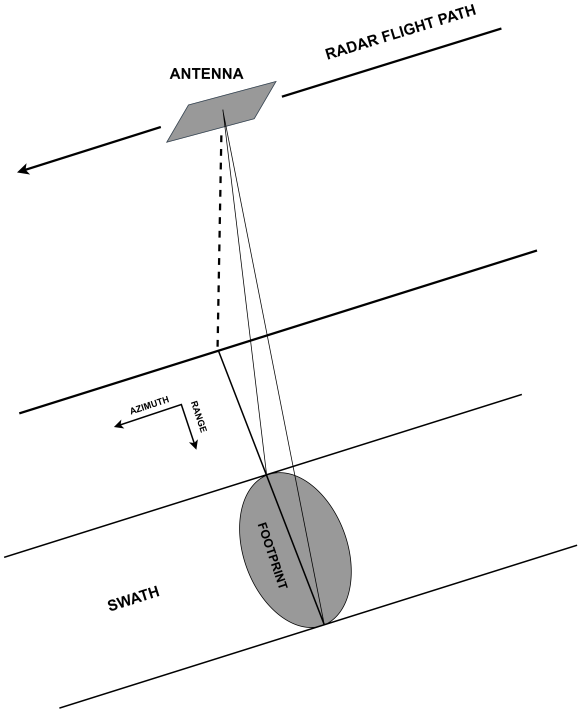

Figure 2: SAR imaging configuration

SAR that are exploited in this work is the amplitude image itself (used for geolocation) and the corresponding range information. An important quantity that one can retrieve from SAR data is the slant range (or line-of-sight distance) from the antenna to a pixel on the ground. For example, the slant range to the center pixel of an image can be written as,

$$\text{Slant Range} = r_0 + (k_c - 1)dr \tag{1}$$

where k_c is the index of the center range line and r_0 is the measured near range. The range spacing is calculated as,

$$dr = \frac{c}{2}\frac{1}{f_s} \tag{2}$$

where c is the speed of light and f_s radar range sample frequency.

SAR Image Formation

The basic raw data needed for generating a SAR image is an array of complex valued pixels that contain magnitude and phase information. Additionally, radar system parameters along with the platform velocity and antenna pointing is also required for proper processing. The processing technique used in this work is an approach where a matched filter is applied on the data to resolve an image. The first step is to compress each radar echo in the range direction. Next, in the azimuth direction the data is Fourier transformed and a matched filter is applied. The matched filter is created from radar parameters, such as pulse repetition frequency and wavelength, in addition to flight parameters. After the matched filter is applied, the complex single-look image is retrieved by inverse Fourier transforming the data in the azimuth direction. Simply taking the amplitude of each pixel yields the amplitude image. More details of the SAR image processing technique can be found in Reference 15.

There are many important parameters that are needed to form an image, including accurate information about the platform's orbit such as its in-track velocity. Additionally, if there are significant out of track velocities the image may become defocused if techniques such as autofocusing are not applied. If image sharpness is significantly degraded due to incorrect knowledge of in-track velocity, subsequent geolocation steps can fail leading to the absence of filter measurement updates. In this paper it is assumed that degradation of SAR image quality only arises from in-track velocity errors and that any antenna pointing errors are small enough to have negligible impact on image quality. Two SAR images are seen in the figure below demonstrating the effects of in-track velocity error. Both are generated from L-band ALOS PALSAR data (available at the Alaska Satellite Facility Distributed Active Archive Center[16]) collected over the Houston area of the United States. This ALOS data has accurate orbit information which nominally produces focused images. To generate the image with in-track error, certain parameters in the processing software are altered to perturb the assumed in-track velocity by 15 m/s. To alleviate these type of errors, a hill climbing algorithm

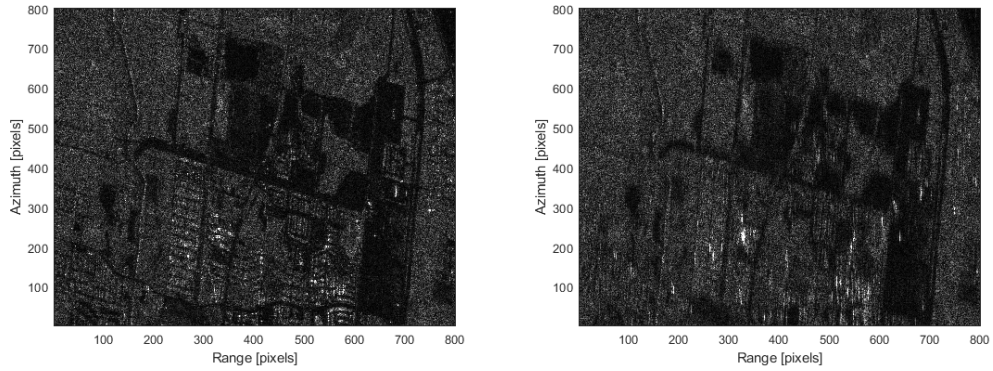

(a) No in-track error

(b) 15 m/s in-track error

Figure 3: Impact of in-track velocity error on SAR image quality

is used to find an in-track velocity value that maximizes the resulting image sharpness. The sharpness metric used for focusing is normalized variance,[17]

$$\text{Sharpness} \equiv \frac{1}{MN\bar{g}^2}\sum_M\sum_N \left[g(i,j) - \bar{g}\right]^2 \tag{3}$$

where the image is $M \times N$ pixels with an individual pixel intensity, $g(i, j)$, and an average pixel intensity $\bar{g}$. A representative image sharpness curve is seen in Figure 4.

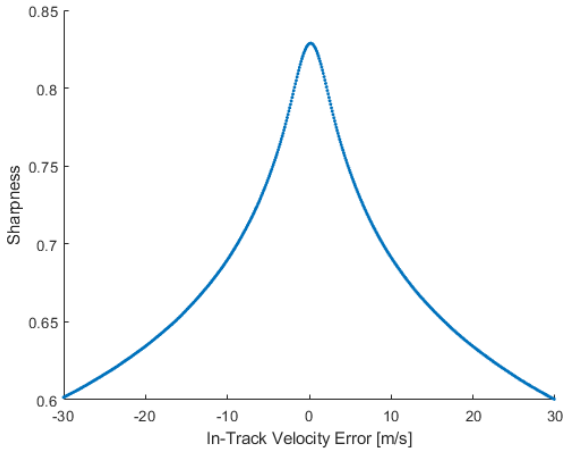

Figure 4: Image sharpness curve

Hill climbing algorithms are a class of derivative-free optimization methods. The hill climbing algorithm functions by "stepping" in the direction that maximizes a cost function, normalized variance in this case, until no more improvement is gained. The constant velocity step size is treated as a user selected parameter that is chosen based on how much in-track velocity error is expected and the allowable computation time of focusing.

Autofocus is a key step of the proposed navigation system. It serves to de-correlate the measurement errors (extracted from a SAR image) from the state estimation errors (the navigation state is used to form the images). The consistency of the EKF implementation shown in the numerical results section of this paper demonstrate that the correlation is effectively mitigated by this approach.

IMAGE GEOLOCATION

Geolocation of the formed SAR image is done by co-registering it to a stored geocoded reference amplitude SAR image. This reference image covers a much larger general area of where the formed image is approximately expected to be. A geocoded SAR image refers to an image in which each pixel has an associated latitude and longitude.

To co-register the two images with each other, features need to be detected in both images and then subsequently matched. This is accomplished by using MATLAB's computer vision toolbox.[18] The Speeded Up Robust Features (SURF) point detector and descriptor is used.[19] This algorithm is both scale and rotation-invariant making it a good choice for this application as the formed image will always cover a much smaller land area than the reference and will often not have the same orientation. The basic input of the algorithm is a grayscale image and the output is an array of SURF features which include characteristics such as point locations, scale, strength, and orientation. The first step of the geolocation process is to detect SURF features in each grayscale image.

After the SURF feature points are detected, putative point matches are made which may include outliers, or features that have a low likelihood of being correctly matched. The geometric transformation (mapping of inliers of one image to another) between the formed image and reference image is then found using the `estimateGeometricTransform` function in the toolbox which eliminates outliers using a random sample consensus algorithm. More details about this specific algorithm can be found in Torr et al.[20] The type of transformation can be specified and for this application an affine transformation is selected. An affine transformation requires a minimum of three matched pairs of features, or the process will fail. Finally, using

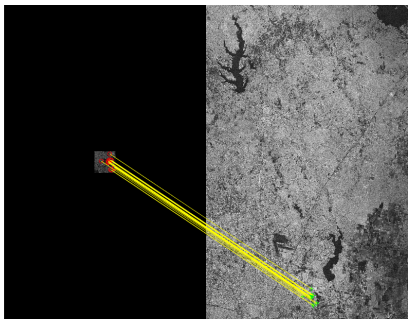

(a) Matched features between the formed and reference SAR images

(b) SAR image bounding box and centroid

Figure 5: Co-registration of SAR images

the transformation from the matched features, a bounding box on the reference image can be drawn. The nearest pixel to the location of the bounding box centroid is found, from which a latitude and longitude is retrieved, as the reference image is geocoded. The matched features and bounding box are seen in Figure 5. It is important to note that feature detection algorithms such as SURF and scale-invariant feature transform (SIFT) can be sensitive to speckle noise from images acquired at different times and that other methods of co-registration exist such as using complex correlation.[21,22]

The latitude and longitude of a location on Earth is not enough to uniquely identify it, as its elevation is also needed. A stored digital elevation map of the larger area is used to determine the elevation of the point of interest. A search is used to find the pixel on the DEM that is closest to the latitude and longitude of the center point. The corresponding height above the WGS 84 ellipsoid is then retrieved. Now with the latitude, longitude, and height (LLH) of the center pixel of the SAR image known, the ECEF coordinate of that point can be calculated using one of several methods of LLH to ECEF conversion.

MULTIPLICATIVE EXTENDED KALMAN FILTER

A 10 component (shown in Table 1) multiplicative extended Kalman filter is employed to estimate the states of the spacecraft. In this paper, states without subscripts or super scripts, such as $\mathbf{r}$ and $\mathbf{v}$, are assumed

Table 1: Estimated states

State	# of Elements	Description
$\mathbf{r}$	3	spacecraft position in ECEF frame
$\mathbf{v}$	3	spacecraft velocity in ECEF frame
$\mathbf{q}_{\mu}$	4	SAR antenna misalignment with spacecraft body quaternion

to be expressed in the ECEF frame. For example, $\mathbf{r}$ is a vector from the center of the earth to the spacecraft expressed in the ECEF frame. Subscripts and superscripts are also used, such as: $\mathbf{r}^{c}_{\mathrm{a,b}}$. This would describe a vector from point a to b expressed in the c frame.

The notation used throughout this paper is to define $\mathbf{q}_a^b$ as the relative orientation quaternion between frames a and b. The quaternion is written as:

$$\mathbf{q}_a^b = \begin{bmatrix} \left(\mathbf{q}_{a,v}^b\right)^T & q_{a,s}^b \end{bmatrix}^T \tag{4}$$

where $\mathbf{q}_{a,v}^b$ is the vector component and $q_{a,s}^b$ is the scalar component. The quaternion product, $\otimes$, that is adopted is Shuster's convention where rotations are interpreted as passive.[23] This is in the opposite order of Hamilton's composition, $\circledast$, where the rotations are treated as active.[24] The two differing compositions are related as follows,

$$\mathbf{p} \otimes \mathbf{q} = \mathbf{q} \circledast \mathbf{p} = \begin{bmatrix} p_s\mathbf{q}_v + q_s\mathbf{p}_v - \mathbf{p}_v \times \mathbf{q}_v \\ p_s q_s - \mathbf{p}_v \cdot \mathbf{q}_v \end{bmatrix}. \tag{5}$$

The direction cosine matrix (DCM), otherwise known as a transformation matrix, can be obtained from a quaternion $\mathbf{q}$:

$$\mathbf{T}(\mathbf{q}) = \left(q_s^2 - \mathbf{q}_v^T\mathbf{q}_v\right)\mathbf{I}_{3\times 3} + 2\mathbf{q}_v\mathbf{q}_v^T - 2\mathbf{q}_s\left[\mathbf{q}_v\times\right], \tag{6}$$

where $[\mathbf{q}_v\times]$ is the skew-symmetric cross product equivalent matrix of the vector components of $\mathbf{q}$,

$$[\mathbf{q}_v\times] = \begin{bmatrix} 0 & -q_3 & q_2 \\ q_3 & 0 & -q_1 \\ -q_2 & q_1 & 0 \end{bmatrix}. \tag{7}$$

An EKF is chosen due to the nonlinear spacecraft dynamics and nonlinear measurement model used. The multiplicative EKF uses the non-singular quaternion representation of attitude, while deviations from the reference are three-component representations.[25] A number of simplifications are made regarding the geometry of the antenna in relation to the spacecraft. It is assumed that the antenna is rigidly attached to the spacecraft and that the center of the antenna is co-located with the center of mass of the vehicle. Additionally, the look and squint angles of the antenna are assumed to be known with some associated uncertainty (misalignment) yielding the nominal transformation between the antenna frame and spacecraft body frame. The look angle is measured from nadir up to the radar beam center, while the squint angle is measured from radar beam center to the normal of the flight path. The attitude of the spacecraft is assumed to be aligned with the local vertical, local horizontal (LVLH) frame at all times in its orbit and is known from an attitude determination system (ADS). Assuming a star-camera/gyro ADS, an attitude error on the order of tens of arcseconds is neglected by this study. Finally, the IMU is also located at the center of mass of the spacecraft and is perfectly aligned with the coordinate system of the spacecraft body. In the context of this filter, "measurements" are gathered from the SAR instrument (and associated autofocusing) and not from the IMU or ADS. These are collected at fixed time increments which are much more spread apart than the high rate output of the IMU and ADS. Below, a three measurement collection is shown where measurement updates only occur at t_1, t_2, and t_3.

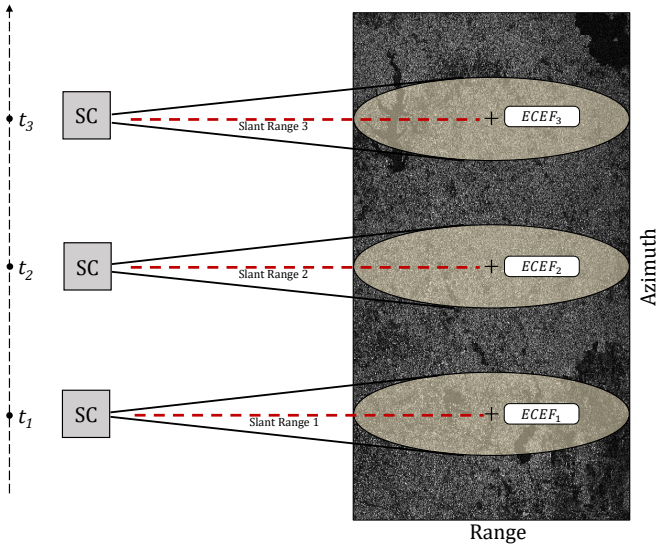

Figure 6: Top view of SAR image collection

Time Propagation

Between SAR derived measurements, the states are propagated with IMU data in a process known as dead-reckoning. Since the position and velocity states are expressed in the ECEF frame, they are propagated in that same frame. This process is often referred to as ECEF mechanization and it is outlined below.[26] Propagation occurs discretely, where the time step, Δt, is the time difference between successive IMU/ADS measurements. Attitude information is received at fixed time increments from the ADS in terms of the quaternion from the ECEF frame to the body frame, $\mathbf{q}_e^b$, which is then converted to the corresponding DCM, $\mathbf{T}_e^b$, for use in subsequent calculations.

Next, the spacecraft acceleration in the ECEF frame, $\mathbf{a}_e$, is expressed as:

$$\mathbf{a}_{\mathrm{e}} = \left(\mathbf{T}_e^b\right)^T \mathbf{a}_{\mathrm{b}} - 2\boldsymbol{\omega}_{\mathrm{ie}}^e \times \hat{\mathbf{v}}_{k-1}^+ + \mathbf{g}_{\mathrm{l}} \tag{8}$$

where $\mathbf{a}_b$ is the measured body acceleration, which is nominally zero in orbit when no maneuvers are occurring and $\boldsymbol{\omega}_{\mathrm{ie}}^e$ is the rotation rate of the earth expressed in the ECEF frame. The hat notation is used to show that a quantity is filter estimate and the minus/plus notations are used to show that the quantity is before/after the measurement update. The local gravity vector, $\mathbf{g}_{\mathrm{l}}$, is the sum of mass attraction acceleration, $\mathbf{g}$, and centripetal acceleration such that:

$$\mathbf{g}_{\mathrm{l}} = \mathbf{g} - \boldsymbol{\omega}_{\mathrm{ie}}^e \times \left[\boldsymbol{\omega}_{\mathrm{ie}}^e \times \hat{\mathbf{r}}_{k-1}^+\right]. \tag{9}$$

Velocity is updated using the previous estimate of the velocity with the acceleration calculated in Eq. (8),

$$\hat{\mathbf{v}}_k^- = \hat{\mathbf{v}}_{k-1}^+ + \mathbf{a}_{\mathrm{e}}\Delta t. \tag{10}$$

Integrating the above equation, position is updated according to,

$$\hat{\mathbf{r}}_k^- = \hat{\mathbf{r}}_{k-1}^+ + \hat{\mathbf{v}}_{k-1}^+\Delta t + \frac{1}{2}\mathbf{a}_{\mathrm{e}}\Delta t^2. \tag{11}$$

The antenna misalignment is a state that does not vary with time, thus it remains unchanged in the time propagation step.

The error covariance matrix, $\mathbf{P}$, is also updated in discrete time according to:

$$\mathbf{P}_k^- = \mathbf{F}_{k-1}\mathbf{P}_{k-1}^+\mathbf{F}_{k-1}^T + \mathbf{G}_{k-1}\mathbf{Q}_{\text{PSD}}\mathbf{G}_{k-1}^T\Delta t \tag{12}$$

where $\mathbf{Q}_{\text{PSD}}$ is a 6×6 diagonal matrix populated by the power spectral densities (PSDs) of the zero-mean Gaussian processes noise. Details of computing the error state matrix $\mathbf{F}$ and input mapping matrix $\mathbf{G}$ can be found in Reference 27.

Measurement Model

After the autofocus and geolocation process, the center pixel of the SAR image has an associated ECEF coordinate and is used for the measurement update. This is in addition to the slant range to the center pixel and the in-track velocity estimate from autofocusing. The measurement vector, $\mathbf{y}$, is seen below,

$$\mathbf{y} = \begin{bmatrix} \phi_{m,1} \\ \phi_{m,2} \\ \|\mathbf{r}_{\text{s,f}}\| \\ v_{ic} \end{bmatrix} \tag{13}$$

where the individual measurement models will subsequently be explained in detail.

Two vector component ratios in the SAR radar frame are extracted from the geolocated image using the following method. First, the relative vector in the ECEF frame from the spacecraft to the center pixel feature of the SAR image is found:

$$\mathbf{r}_{\text{s,f}} = \mathbf{r}_{\text{f}} - \hat{\mathbf{r}}. \tag{14}$$

A graphic representation of these vectors can be seen in Figure 7. The relative position vector, $\mathbf{r}_{\text{s,f}}$, is then

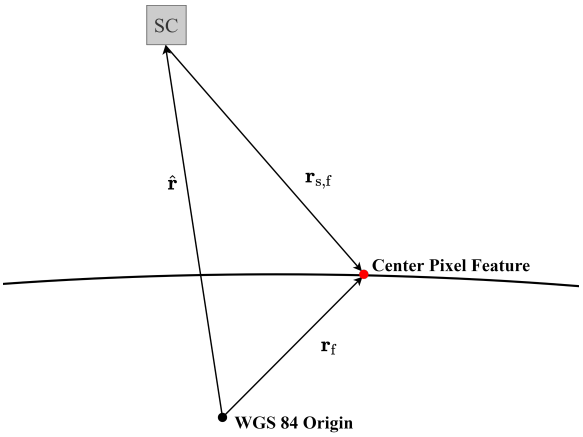

Figure 7: Measurement vectors

expressed in the SAR antenna frame using the spacecraft attitude, estimated antenna misalignment DCM, $\hat{\mathbf{T}}_\mu$, and nominal DCM between spacecraft body frame and antenna frame, $\mathbf{T}_b^s$,

$$\mathbf{r}_{\text{s,f}}^s = \hat{\mathbf{T}}_\mu\mathbf{T}_b^s\mathbf{T}_e^b\mathbf{r}_{\text{s,f}} \tag{15}$$

where the superscript, s, on the position vector indicates that it is expressed in the antenna frame. The DCM $\mathbf{T}_b^s$ is constructed from the nominal radar look and squint angles.

The two ratio measurements can then be easily computed from $\mathbf{r}_{\text{s}}^s$ such that,

$$\phi_{m,1} = \frac{x_{\text{s}}}{z_{\text{s}}}, \quad \phi_{m,2} = \frac{y_{\text{s}}}{z_{\text{s}}} \tag{16}$$

where $\begin{bmatrix} x_\mathrm{s} & y_\mathrm{s} & z_\mathrm{s} \end{bmatrix}^T$ are simply the components of $\mathbf{r}^s_{\mathrm{s,f}}$. From this construction, it is clear that all measurements of this type will nominally be zero due to $\mathbf{r}^s_{\mathrm{s,f}}$ only having non-zero values in the z-axis, while the predicted measurements in the filter will always be non-zero due to imprecise knowledge of the states.

Next, the predicted slant range to the center pixel feature is simply,

$$\text{Slant Range} \equiv \|\mathbf{r}_{\mathrm{s,f}}\| \,. \tag{17}$$

The last component of the measurement vector is in-track velocity. For the purposes of this work, it is assumed that the orbit is perfectly circular, thus the in-track velocity is equal to the magnitude of the velocity vector. This results in the following relationship between the in-track spacecraft velocity and the ECEF spacecraft velocity:

$$v_{ic} = \|\mathbf{v}\| \,. \tag{18}$$

Equations 16, 17, and 18 make up the measurement model $h(\mathbf{x})$ to be used in the measurement update of the MEKF.

Measurement Update

In the event that a SAR derived measurement is collected, an MEKF measurement update is performed where the first step is to calculate $\mathbf{H}_k$.

The observation model matrix, $\mathbf{H}_k$, is found by calculating the following Jacobian,

$$\mathbf{H}_k = \frac{\partial h(\mathbf{x})}{\partial \mathbf{x}}\Big|_{\mathbf{x}=\hat{\mathbf{x}}_k^-}. \tag{19}$$

The ratio measurement Jacobian with respect to position can be written as,

$$\frac{\partial \boldsymbol{\phi}_m}{\partial \mathbf{r}} = \frac{\partial \boldsymbol{\phi}_m}{\partial \mathbf{r}^s_{\mathrm{s,f}}} \frac{\partial \mathbf{r}^s_{\mathrm{s,f}}}{\partial \mathbf{r}} \tag{20}$$

where

$$\frac{\partial \boldsymbol{\phi}_m}{\partial \mathbf{r}^s_{\mathrm{s,f}}} = \begin{bmatrix} 1/z_\mathrm{s} & 0 & -x_\mathrm{s}/z_\mathrm{s}^2 \\ 0 & 1/z_\mathrm{s} & -y_\mathrm{s}/z_\mathrm{s}^2 \end{bmatrix} \tag{21}$$

and

$$\frac{\partial \mathbf{r}^s_{\mathrm{s,f}}}{\partial \mathbf{r}} = -\mathbf{T}_\mu \mathbf{T}^s_b \mathbf{T}^b_e. \tag{22}$$

The slant range measurement is only a function of vehicle position and results in the Jacobian:

$$\frac{\partial \|\mathbf{r}_{\mathrm{s,f}}\|}{\partial \mathbf{r}} = -\frac{1}{\|\mathbf{r}_{\mathrm{s,f}}\|} \left(\mathbf{r}_{\mathrm{s,f}}\right)^T . \tag{23}$$

Similarly, the in-track velocity measurement is only a function of the spacecraft's velocity resulting in,

$$\frac{\partial v_{ic}}{\partial \mathbf{v}} = \frac{1}{\|\mathbf{v}\|} \left(\mathbf{v}\right)^T . \tag{24}$$

Finally, the Jacobian of the ratios with respect to the antenna misalignment error $\delta\boldsymbol{\mu}$ is computed from the first-order approximation of the error-attitude matrix,[28]

$$\mathbf{T}\left(\delta\mathbf{q}_\mu\right) \approx \mathbf{I}_{3\times 3} - \left[\delta\boldsymbol{\mu}\times\right], \tag{25}$$

yielding the Jacobian

$$\frac{\partial \boldsymbol{\phi}_m}{\partial \delta \boldsymbol{\mu}} = \frac{\partial \boldsymbol{\phi}_m}{\partial \mathbf{r}^s_{\mathrm{s,f}}} \frac{\partial \mathbf{r}^s_{\mathrm{s,f}}}{\partial \delta \boldsymbol{\mu}}, \tag{26}$$

where

$$\frac{\partial \mathbf{r}^s_{\mathrm{s,f}}}{\partial \delta \boldsymbol{\mu}} = \left[\mathbf{T}_\mu \mathbf{T}^s_b \mathbf{T}^b_e \mathbf{r}_{\mathrm{s,f}} \times \right]. \tag{27}$$

The resulting 4×9 $\mathbf{H}_k$ matrix is

$$\mathbf{H}_k = \begin{bmatrix} \frac{\partial \boldsymbol{\phi}_m}{\partial \mathbf{r}} & \mathbf{O}_{2\times3} & \frac{\partial \boldsymbol{\phi}_m}{\partial \delta \boldsymbol{\theta}} \\ \frac{\partial \|\mathbf{r}_{\mathrm{s,f}}\|}{\partial \mathbf{r}} & \mathbf{O}_{1\times3} & \mathbf{O}_{1\times3} \\ \mathbf{O}_{1\times3} & \frac{\partial v_{ic}}{\partial \mathbf{v}} & \mathbf{O}_{1\times3} \end{bmatrix}. \tag{28}$$

Due to the measurement model employed, not all uncertainties involved are properly captured using the standard EKF implementation. Mainly, the uncertainty of the geolocation process of the SAR image is not accounted for in the measurement covariance matrix, $\mathbf{R}$, which is a diagonal matrix consisting of vector ratio, slant range, and in-track velocity errors. To account for this, a matrix, $\mathbf{B}$, is defined such that,

$$\mathbf{B}_k = \tilde{\mathbf{H}}_k \mathbf{D} \tilde{\mathbf{H}}_k^T \tag{29}$$

where $\mathbf{D}$ is the center pixel covariance matrix and $\tilde{\mathbf{H}}_k$ is the Jacobian of the measurement model with respect to the SAR image center pixel $\mathbf{r}_{\mathrm{f}}$:

$$\tilde{\mathbf{H}}_k = \frac{\partial h(\mathbf{x})}{\partial \mathbf{r}_{\mathrm{f}}}\Big|_{\mathbf{x}=\hat{\mathbf{x}}_k^-} = \begin{bmatrix} -\frac{\partial \boldsymbol{\phi}_m}{\partial \mathbf{r}} \\ -\frac{\partial \|\mathbf{r}_{\mathrm{s,f}}\|}{\partial \mathbf{r}} \\ \mathbf{O}_{1\times3} \end{bmatrix}. \tag{30}$$

This is then included in the formulation of the innovation covariance.

The extended Kalman filter neglects higher order effects of nonlinear measurement models due to the first order Taylor approximation it utilizes. This can often cause the estimated error covariance to update too "aggressively" and become inconsistent with the true estimation error in the presence of highly accurate measurements combined with large *a priori* uncertainty.[29] Underweighting measurements is a method to account for these higher order effects by artificially increasing the measurement error to achieve consistency during filtering. Lear's method[30] accomplishes this by scaling the $\mathbf{HPH}^T$ term of the innovation covariance which accounts for the uncertainty in the states. This leads to an innovation covariance at time k of:

$$\mathbf{S}_k = \begin{cases} (1+\bar{\beta})\mathbf{H}_k \mathbf{P}_k^- \mathbf{H}_k^T + \mathbf{R} + \mathbf{B}_k \,, & \text{if } \sqrt{\mathrm{tr}(\mathbf{P}^-_{i,k})} > \gamma \\ \mathbf{H}_k \mathbf{P}_k^- \mathbf{H}_k^T + \mathbf{R} + \mathbf{B}_k \,, & \text{otherwise} \end{cases} \tag{31}$$

where $\bar{\beta}$ and γ are tuning parameters, while $\mathbf{P}^-_{i,k}$ is a chosen partition (such as position states) of the estimation error covariance matrix. Initiating underweighting based on the partitioned covariance matrix is just one method of many. For example, one could also apply underweighting for the first n measurements after a long time span without measurement updates.

The Kalman gain is then calculated,

$$\mathbf{K}_k = \mathbf{P}_k^- \mathbf{H}_k^T \mathbf{S}_k^{-1} \tag{32}$$

and,

$$\Delta \hat{\mathbf{x}}_k = \begin{bmatrix} \Delta \hat{\mathbf{r}}_k \\ \Delta \hat{\mathbf{v}}_k \\ \delta \hat{\boldsymbol{\mu}}_k \end{bmatrix} = \mathbf{K}_k \tilde{\mathbf{y}}_k \tag{33}$$

where $\tilde{\mathbf{y}}_k$ is the pre-fit residual. Position and velocity states are updated additively:

$$\hat{\mathbf{r}}_k^+ = \hat{\mathbf{r}}_k^- + \Delta \hat{\mathbf{r}}_k \tag{34}$$

$$\hat{\mathbf{v}}_k^+ = \hat{\mathbf{v}}_k^- + \Delta\hat{\mathbf{v}}_k, \tag{35}$$

while the antenna misalignment quaternion is updated multiplicatively and re-normalized,

$$\hat{\mathbf{q}}_{\mu_k}^+ = \delta\hat{\mathbf{q}}_{\mu_k} \otimes \hat{\mathbf{q}}_{\mu_k}^-, \tag{36}$$

with $\delta\hat{\mathbf{q}}_{\mu_k}$ defined as,

$$\delta\hat{\mathbf{q}}_{\mu_k} = \begin{bmatrix} \frac{\delta\hat{\boldsymbol{\mu}}_k}{\|\delta\hat{\boldsymbol{\mu}}_k\|} \sin\left(\frac{1}{2}\|\delta\hat{\boldsymbol{\mu}}_k\|\right) \\ \cos\left(\frac{1}{2}\|\delta\hat{\boldsymbol{\mu}}_k\|\right) \end{bmatrix}. \tag{37}$$

The covariance matrix is updated using the Joseph form to maintain symmetry and definiteness.

$$\mathbf{P}_k^+ = (\mathbf{I}_{9\times 9} - \mathbf{K}_k\mathbf{H}_k)\,\mathbf{P}_k^-\,(\mathbf{I}_{9\times 9} - \mathbf{K}_k\mathbf{H}_k)^T + \mathbf{K}_k\mathbf{R}'\mathbf{K}_k^T \tag{38}$$

To account for the underweighting used above and the addition of uncertainty due to geolocation error, $\mathbf{R}'$ is defined as:

$$\mathbf{R}' = \beta\mathbf{H}_k\mathbf{P}_k^-\mathbf{H}_k^T + \mathbf{R} + \mathbf{B}_k. \tag{39}$$

NUMERICAL SIMULATION

The performance of the system is simulated in two ways, closed-loop and open-loop. The closed-loop simulation processes real SAR data to generate images and derives measurements at every measurement update. The navigation solution is utilized to generate the SAR image and its associated measurements. This is in contrast to the open-loop simulation in which the SAR derived measurements are not actually generated from the methods discussed in the above section, but are simulated with errors in geolocation, in-track velocity, and range. The nominal trajectory used in the simulations and other important parameters are discussed below.

Closed-Loop Trajectory and SAR Data

All closed-loop Monte Carlo simulations use the same real SAR data set and hence the same nominal flight track. Namely, data from the Advanced Land Observing Satellite (ALOS) is used; a remote sensing satellite that was launched in January of 2006 by Japanese Aerospace Exploration Agency. Some of the orbital parameters of ALOS can be seen in Table 2 below.[31]

Table 2: ALOS orbital parameters

Orbital Parameter	Value
Altitude at equator	691.5 km
Inclination	98.16°
Eccentricity	0.00118
Period	98.5 min

A roughly 41 second trajectory from February of 2008 over the Houston area of the United States is chosen for simulation from which three images are retrieved for SAR measurement updates. What are referred here as images are technically two amplitude patches of a larger array of complex values, but for the purposes of this simulation are simply called "images".

The true trajectory of the spacecraft is known extremely well due to high-precision orbit determination performed using a duel-frequency GPS receiver together with ground control points scattered throughout the world. This results in an orbit accuracy of about 40 cm (3σ).[31] A time history of true spacecraft attitude is generated using a multi-step approach. First, 5 pairs of position and velocity vectors are selected at equal time increments encompassing the entire trajectory. For each of these pairs, Wahba's problem is solved using singular value decomposition.[32] This method seeks to find a DCM between two coordinate systems (ECEF

and body in this case) given pairs of weighted vectors. In choosing the pairs, the assumption is that the spacecraft is in an LVLH orientation and in a perfectly circular orbit. The constant spacecraft body rate is then found from the calculated attitude of the spacecraft at different times throughout the flight path and is used to create the true spacecraft attitude to be output from the simulated ADS.

Due to the fact that only one realization of real data is available for this particular orbital pass, the range measurements were corrupted with additional additive Gaussian noise in both the closed-loop simulations.

Open-Loop Trajectory

As discussed in the above section, only three measurement updates are included in the closed-loop trajectory. To evaluate the performance of the system for a longer trajectory (and more measurements) an open-loop simulation is conducted. Since real SAR data is not being used to generate images, synthetic measurements are derived with simulated additive zero-mean Gaussian noise.

The truth trajectory is created by using the same initial conditions as the closed-loop trajectory and propagating it forward in time under central gravity and J_2 perturbation. The spacecraft attitude is found by propagating the constant body rate previously found. This extended trajectory spans 10 minutes and the boresight ground track originates from Houston (as in the closed-loop trajectory) ascending to northern Canada.

Simulated SAR measurements are retrieved at the same interval as the closed-loop trajectory, totaling 72 measurement updates over the 10 minute trajectory. To simulate the geolocation of the center SAR image pixel, $\mathbf{r}_{\text{f}}$, the (near side) intersection of a ray along the boresight of the SAR antenna and the WGS 84 ellipsoid is found at each of the measurement update times. This is done with knowledge of the true spacecraft position, attitude, and SAR pointing angles. While in the closed-loop trajectory elevation values vary, it is assumed that all feature points in the open-loop simulation are at zero elevation above the reference ellipsoid. From this, applying the proper additive Gaussian white noise yields a simulated ground center feature which can be used to calculate the two ratio measurements. Additionally, from the truth ground center feature a simulated range measurement is calculated, again with the addition of appropriate noise. Finally, instead of relying on an autofocusing algorithm for v_{ic}, the magnitude of the true velocity vector is simply calculated and noise added to simulate the measurement.

MEKF Parameters

During the time propagation step of the filter, only central gravity and J_2 perturbation are modeled. It is assumed that the accelerometers onboard are not sensitive enough to measure non-gravitational forces acting on the spacecraft and thus the measured body acceleration by the IMU, $\mathbf{a}_{\text{b}}$, is dominated by noise. Perturbing effects such as solar radiation pressure and atmospheric drag act on the spacecraft, and are accounted for in process noise added to the filter during time propagation, yielding the power spectral density matrix of,

$$\mathbf{Q}_{\text{PSD}} = \begin{bmatrix} 3.5 \times 10^{-11}\mathbf{I}_{3\text{x}3} & \mathbf{O}_{3\text{x}3} \\ \mathbf{O}_{3\text{x}3} & 3.4 \times 10^{-13}\mathbf{I}_{3\text{x}3} \end{bmatrix}$$

with process noise for the antenna misalignment states accounting for noise in the true data.

Next, the measurement covariance matrix, $\mathbf{R}$, is defined which includes the uncertainty of the two ratios, slant range, and in-track velocity measurements. It is shown below,

$$\mathbf{R} = \begin{bmatrix} \sigma^2_{\phi_{m,1}} & 0 & 0 & 0 \\ 0 & \sigma^2_{\phi_{m,2}} & 0 & 0 \\ 0 & 0 & \sigma^2_{\text{range}} & 0 \\ 0 & 0 & 0 & \sigma^2_{v_{ic}} \end{bmatrix}$$

with the respective noise standard deviations seen in Table 3.

As discussed in the measurement model section in the previous section, the two vector component ratios are always identically zero, as the antenna boresight is aligned with the antenna frame z-axis. For the range

Table 3: Measurement noise

	Value	Units
$\sigma_{\phi_{m,1}}$	0	[-]
$\sigma_{\phi_{m,2}}$	0	[-]
σ_{range}	1	m
$\sigma_{v_{ic}}$	0.54	m/s

measurement, no data is available for the range uncertainty of the SAR instrument on ALOS, but 1 meter is chosen as this is a conservative 1σ accuracy for a radar of this type. The in-track velocity output uncertainty is obtained from experimental results of the auto-focusing algorithm outputs for a Monte Carlo simulation of the first measurement in the trajectory. It is important to note that this value is highly dependent on the step size used for focusing, with small steps yielding more accurate in-track velocity measurements. For the closed-loop simulation this step size is fixed at 1 m/s.

Similarly to the uncertainty of the in-track velocity measurement, the center pixel covariance matrix, **D**, introduced in Equation 29 is found using Monte Carlo simulations of the first measurement with ECEF uncertainty ranging from 2 to 8 meters 1σ. This covariance matrix accounts the uncertainty due to the geolocation process and is used to generate zero mean additive Gaussian noise to simulate geolocation error in the open-loop simulation. In reality, it is likely that this geolocation error is position dependent in regards to the amount of error in each direction due to the view of the ECEF coordinate system changing from the perspective of the SAR antenna. For the purposes of this paper, it is assumed that this geolocation covariance matrix is constant. Additionally, minor bias is found in the geolocation process (on the order of a single pixel) and is compensated for in the filter.

Underweighting is only utilized in test case 1, as it is found to be necessary in that scenario only. A description of the two test cases is discussed in a later section. In test case 1, underweighting of measurements is applied based on the measurement index and not the filter's predicted uncertainty. The first 10 measurements are chosen to have underweighting applied as this is when filter inconsistency is most likely to occur due to the reception of low uncertainty measurements after a period lacking any measurements. Since the closed-loop simulation only has three measurement updates, each of them has underweighting applied for test case 1. The underweighting parameter, $\bar{\beta}$, is chosen to be 0.2, the same value used for the Space Shuttle.[30]

TEST CASES

Two test cases are simulated which only differ in the uncertainty of the initial state estimates, while keeping all other parameters discussed in the previous sections identical. Specifically, both cases begin with the same initial uncertainty for the position and velocity states, but a different uncertainty for the initial antenna misalignment. A table of the initial estimation errors of the two test cases is seen below. This uncertainty is applied to all components of the respective states.

Table 4: Initial estimation error

State	TC-1 Initial Uncertainty [1σ]	TC-2 Initial Uncertainty [1σ]	Units
$\mathbf{r}$	1000	1000	m
$\mathbf{v}$	10	10	m/s
$\boldsymbol{\mu}$	0.1	0.01	deg

Monte Carlo Results

Two sets of plots are shown for the test case 1 scenario, where sample statistic results are constructed from 100 Monte Carlo runs. Figures 8a - 8c show results of the closed-loop simulation for three measurement

updates where the error of each run is shown as a gray line with the dashed black line representing the sample mean of the estimation error. This mean error is nearly zero throughout the trajectory meaning the filter produces unbiased estimates. The filter predicted estimation error covariance (3σ) is plotted with the sample error covariance (3σ) in red and green respectively. The sample covariance shows the true error characteristics, which the filter attempts to estimate. When these two covariances match closely, the filter is said to be consistent and this can be seen in the figures as well. Although not explicitly shown, there is good agreement between the closed-loop and open-loop simulation results for the measurements that are common to both.

Figures 9a - 9c show the same information as Figures 8a - 8c except now the open-loop trajectory is shown for the full 10 minute time span. The sample and predicted covariances generally have good agreement except for the beginning of the trajectory for the velocity states where the filter slightly outperforms its predicted covariance. At the end of the trajectory the uncertainty (1σ) for the ECEF position ranges from roughly 20 meters in the x-axis to 740 meters in the y-axis, a 98% and 26% decrease respectively.

The same sets of figures is presented for test case 2 as is presented in test case 1. In Figures 10a - 10c the closed-loop simulation results show unbiased estimation along with acceptable filter consistency. Additionally, while again not shown, there is good agreement between the open-loop and closed-loop simulation as the sample uncertainties of the first three measurements match closely. Finally, Figures 11a - 11c show unbiased estimation and good consistency throughout the 10 minute open-loop trajectory. The ECEF positional uncertainty (1σ) at the end of the trajectory ranges from 12 meters in the x-axis to 138 meters in the y-axis, a 98.8% and 86.2% decrease respectively. As expected, for both test cases, antenna misalignment uncertainty around the antenna z-axis (boresight) does not decrease due to the lack of observability of this component because of measurement types employed. The largest difference between the two test cases that can be seen is that when the initial antenna misalignment uncertainty is low (as in test case 2) the position and velocity state errors decrease rapidly to their steady state values, while antenna misalignment uncertainty only decreases slightly during this 10 minute section of the orbit.

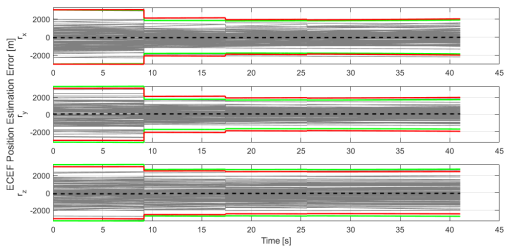

(a) Position estimation

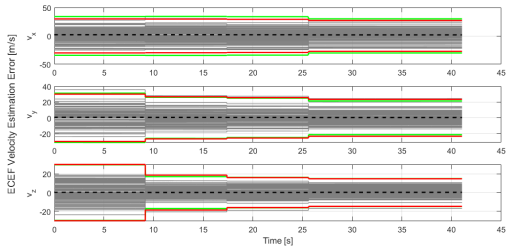

(b) Velocity estimation

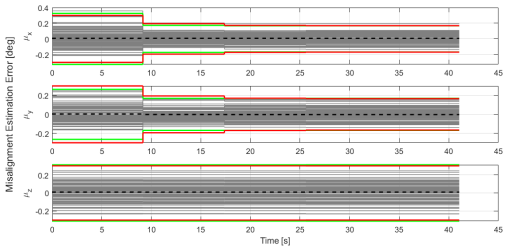

(c) Antenna misalignment estimation

Figure 8: Monte Carlo results of closed-loop estimation error (TC-1)

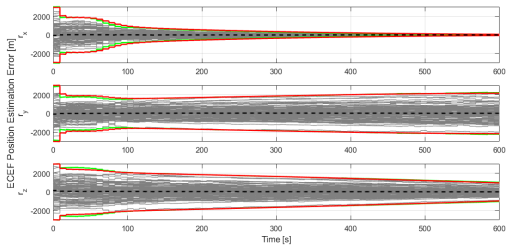

(a) Position estimation

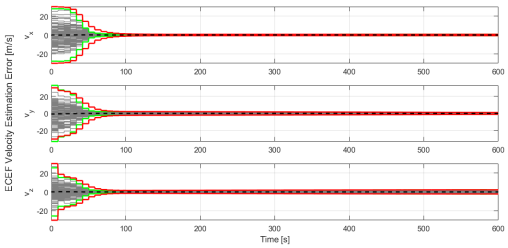

(b) Velocity estimation

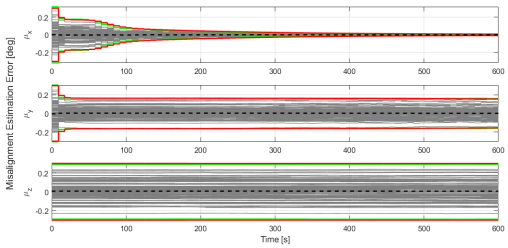

(c) Antenna misalignment estimation

Figure 9: Monte Carlo results of open-loop estimation error (TC-1)

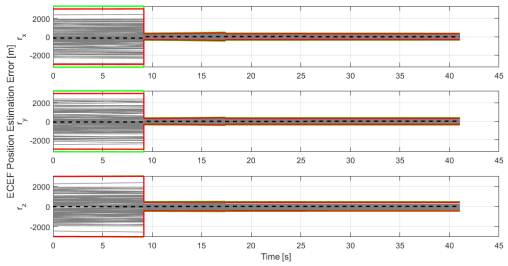

(a) Position estimation

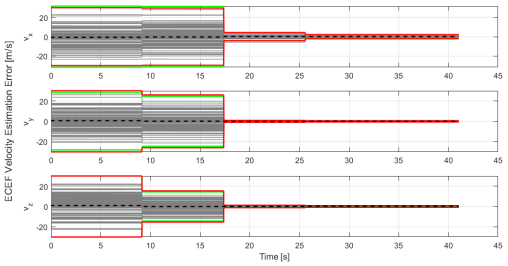

(b) Velocity estimation

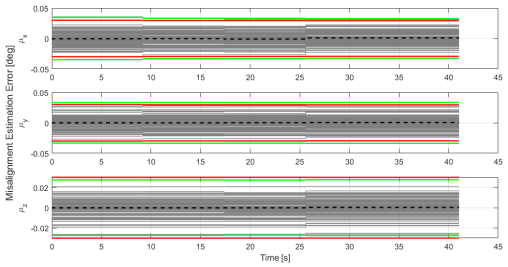

(c) Antenna misalignment estimation

Figure 10: Monte Carlo results of closed-loop estimation error (TC-2)

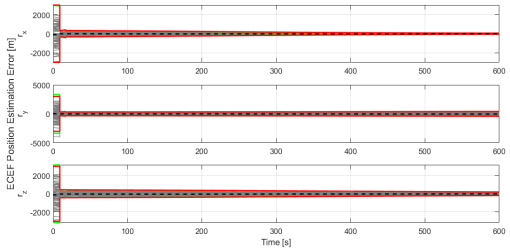

(a) Position estimation

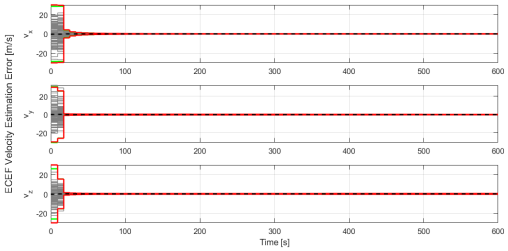

(b) Velocity estimation

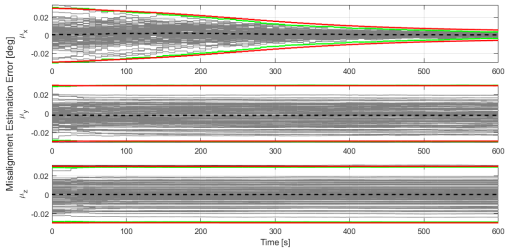

(c) Antenna misalignment estimation

Figure 11: Monte Carlo results of open-loop estimation error (TC-2)

CONCLUSION

A prototype SAR based terrain relative navigation system has been proposed and developed. A key component of this work is the fact that this is a closed-loop navigation architecture where the SAR measurements and navigation filter are reliant on one another. Through Monte Carlo analysis of the MEKF performance for two test cases, it was shown that the filter bounds and often significantly reduces state errors throughout the trajectory. In the comparison of the two test cases, it is clear that a smaller initial antenna misalignment error has a significant contribution to the rate that the other two states' uncertainty decreases, which is an expected result due to the direct downstream coupling of antenna misalignment with position and velocity EKF measurement updates. Future research will aim to relax multiple assumptions outlined in this paper. The most apparent is elimination of the restriction that the spacecraft is in a circular orbit and is always in a perfect LVLH Earth pointing attitude. Additionally, the incorporation of body attitude errors from misalignment and noise in the attitude determination system may more accurately represent real flight scenarios.

ACKNOWLEDGMENT

This research was supported by the Laboratory Directed Research and Development program at Sandia National Laboratories, a multimission laboratory managed and operated by National Technology and Engineering Solutions of Sandia LLC, a wholly owned subsidiary of Honeywell International Inc. for the U.S. Department of Energy's National Nuclear Security Administration under contract DE-NA0003525.

REFERENCES

[1] J. P. Golden, "Terrain contour matching (TERCOM): A cruise missile guidance aid," *Image processing for missile guidance*, Vol. 238, International Society for Optics and Photonics, 1980, pp. 10–18.

[2] T. G. McGee, P. E. Rosendall, A. Hill, W. J. Shyong, T. B. Criss, C. Reed, G. Chavers, M. Hannan, C. Epp, and M. Nishant, "APLNav: Development status of an onboard passive optical terrain relative navigation system," *AIAA Guidance, Navigation, and Control Conference*, 2015, p. 0853.

[3] D. Rutishauser, C. Epp, and E. Robertson, "Free-flight terrestrial rocket lander demonstration for NASA's Autonomous Landing and Hazard Avoidance Technology ALHAT system," *AIAA SPACE 2012 Conference & Exposition*, 2012, p. 5239.

[4] N. Mastrodemos, B. Rush, D. Vaughan, and B. Owen, "Optical navigation for Dawn at Vesta," *21st AAS/AIAA Space Flight Mechanics Meeting*, 2011.
[5] A. E. Johnson and J. F. Montgomery, "Overview of terrain relative navigation approaches for precise lunar landing," *2008 IEEE Aerospace Conference*, IEEE, 2008, pp. 1–10.
[6] F. Amzajerdian, V. E. Roback, A. E. Bulyshev, P. F. Brewster, W. A. Carrion, D. F. Pierrottet, G. D. Hines, L. B. Petway, B. W. Barnes, and A. M. Noe, "Imaging flash LIDAR for safe landing on solar system bodies and spacecraft rendezvous and docking," *Laser Radar Technology and Applications XX; and Atmospheric Propagation XII*, Vol. 9465, International Society for Optics and Photonics, 2015, p. 946502.
[7] G. Born, J. Dunne, and D. Lame, "Seasat mission overview," *Science*, Vol. 204, No. 4400, 1979, pp. 1405–1406.
[8] M. Werner, "Shuttle radar topography mission (SRTM) mission overview," *Frequenz*, Vol. 55, No. 3-4, 2001, pp. 75–79.
[9] D. Geudtner, R. Torres, P. Snoeij, M. Davidson, and B. Rommen, "Sentinel-1 system capabilities and applications," *2014 IEEE Geoscience and Remote Sensing Symposium*, IEEE, 2014, pp. 1457–1460.
[10] J. E. Bevington and C. A. Marttila, "Precision aided inertial navigation using SAR and digital map data," *IEEE Symposium on Position Location and Navigation. A Decade of Excellence in the Navigation Sciences*, IEEE, 1990, pp. 490–496.
[11] R. N. Paschall and J. Layne, "Design and analysis of an integrated targeting system," *Proceedings of National Aerospace and Electronics Conference (NAECON'94)*, IEEE, 1994, pp. 937–944.
[12] A. W. Doerry, "Estimating IMU heading error from SAR images.," tech. rep., Sandia National Laboratories, 2009.
[13] A. W. Doerry, V. Horndt, D. L. Bickel, and R. M. Naething, "Estimating Radar Velocity using Direction of Arrival Measurements," tech. rep., Sandia National Laboratories, 2014.
[14] A. Moreira, P. Prats-Iraola, M. Younis, G. Krieger, I. Hajnsek, and K. P. Papathanassiou, "A tutorial on synthetic aperture radar," *IEEE Geoscience and remote sensing magazine*, Vol. 1, No. 1, 2013, pp. 6–43.
[15] I. G. Cumming and F. H. Wong, *Digital processing of synthetic aperture radar data: algorithms and implementation*. Artech House Norwood, MA, 2005.
[16] JAXA/METI, "ALOS PALSAR L1.0," 2008. Accessed through ASF DAAC 04 April 2020.
[17] F. C. Groen, I. T. Young, and G. Ligthart, "A comparison of different focus functions for use in autofocus algorithms," *Cytometry: The Journal of the International Society for Analytical Cytology*, Vol. 6, No. 2, 1985, pp. 81–91.
[18] MATLAB, *Computer Vision Toolbox*. Natick, Massachusetts, United States: The MathWorks, Inc., 2020.
[19] H. Bay, T. Tuytelaars, and L. Van Gool, "Surf: Speeded up robust features," *European conference on computer vision*, Springer, 2006, pp. 404–417.
[20] P. H. Torr and A. Zisserman, "MLESAC: A new robust estimator with application to estimating image geometry," *Computer vision and image understanding*, Vol. 78, No. 1, 2000, pp. 138–156.
[21] S. Suri, P. Schwind, J. Uhl, and P. Reinartz, "Modifications in the SIFT operator for effective SAR image matching," *International Journal of Image and Data Fusion*, Vol. 1, No. 3, 2010, pp. 243–256.
[22] Z. Li, J. Bethel, *et al.*, "Image coregistration in SAR interferometry," *The International Archives of the Photogrammetry, Remote Sensing and Spatial Information Sciences*, Vol. 37, 2008, pp. 433–438.
[23] M. D. Shuster, "Survey of attitude representations," *Journal of the Astronautical Sciences*, Vol. 41, 1993, pp. 439–517.
[24] R. Zanetti, "Rotations, Transformations, Left Quaternions, Right Quaternions?," *The Journal of the Astronautical Sciences*, Vol. 66, No. 3, 2019, pp. 361–381.
[25] F. L. Markley, "Attitude estimation or quaternion estimation?," *Journal of the Astronautical Sciences*, Vol. 52, No. 1-2, 2004, pp. 221–238.
[26] D. Titterton, J. L. Weston, and J. Weston, *Strapdown inertial navigation technology*, Vol. 17. IET, 2004.
[27] R. Zanetti, *Advanced navigation algorithms for precision landing*. PhD thesis, The University of Texas at Austin, 2007.
[28] J. L. Crassidis and J. L. Junkins, *Optimal estimation of dynamic systems*. CRC press, 2011.
[29] J. R. Carpenter and C. N. D'Souza, "Navigation filter best practices," tech. rep., NASA Langley Research Center, 2018.
[30] W. M. Lear, "Multi-phase navigation program for the Space Shuttle Orbiter," *JSC Internal Note No. 73-FM-132*, 1973.
[31] M. Shimada, T. Tadono, and A. Rosenqvist, "Advanced Land Observing Satellite (ALOS) and monitoring global environmental change," *Proceedings of the IEEE*, Vol. 98, No. 5, 2009, pp. 780–799.
[32] F. L. Markley, "Attitude determination using vector observations and the singular value decomposition," *Journal of the Astronautical Sciences*, Vol. 36, No. 3, 1988, pp. 245–258.